

Competition between correlated buoyancy and uncorrelated capillary effects during drainage

Harold Auradou,^{1,2} Knut Jørgen Måløy,¹ Jean Schmittbuhl,³ Alex Hansen,⁴ and Daniel Bideau²

¹*Fysisk Institutt, Universitetet i Oslo, Postboks 1048 Blindern, N-0316 Oslo, Norway*

²*Groupe Matière Condensée et Matériaux, Université de Rennes 1, F-35042 Rennes Cedex, France*

³*Departement TAO, Ecole Normale Supérieure Paris, 24 rue Lhomond, F-75231 Paris Cedex 05, France*

⁴*Institutt for Fysikk, Norges Teknisk-Naturvitenskapelige Universitet, N-7491 Trondheim, Norway*

(Received 19 May 1999)

We study drainage in a horizontally oriented rough fracture joint filled with glass beads. The shape and structure of the drained areas is the result of competition between two effects: (1) variations in the capillary thresholds necessary to be overcome in order to drain the pores and (2) the height variations due to the roughness of the fracture joint. These height variations have long range correlations due to the self-affine nature of the fracture. The capillary thresholds are uncorrelated. We tune the relative strength of these two effects by performing experiments in a centrifuge and thus changing the “strength of gravity.” As gravity is increased, the structure of the drained areas change from that of invasion percolation to a structure composed of compact blobs linked together by threadlike links. We study both the geometry and the effect of trapping while changing acceleration of gravity from zero to $6g_0$. At high centrifugal acceleration we further observe fragmentation, migration and coalescence of bubbles of fluid inside the drained areas.

[S1063-651X(99)13112-X]

PACS number(s): 47.55.Mh, 05.40.-a, 47.55.Kf, 64.60.Ak

I. INTRODUCTION

Two-phase flow in porous media and fractures is central to many fields including oil recovery, hydrology, soil mechanics, and spreading of contaminations. Recent work has mostly been focused on the study of two phase flow in homogeneous porous media [1–3]. In particular, much attention has been given to the study of the variety of complex structures observed at different physical parameters of the fluids under these conditions. Less focus has been on the effects of heterogeneities such as fractures or permeability variations which introduce long-range correlations in the system.

In this work we describe two-phase flow experiments in a fracture joint filled with a noncrystalline — i.e., disordered — monolayer of glass beads. A nonwetting light fluid displaces a wetting dense fluid at an injection rate which is small enough for viscous effects to be neglected. Long range correlations are introduced through hydrostatic pressure variations due to the height differences of the rough fracture landscape. There is also an uncorrelated component in the model which is due to the capillary pressure thresholds that need to be overcome by the nonwetting fluid to invade the porous monolayer pore after pore. The randomness in the capillary pressure thresholds is due to the way the glass beads have been distributed between the two opposite fracture surfaces.

It is well known that natural fractures are self-affine [4–8]. A self-affine fractal [9] surface, $h(x,y)$, isotropic in the (x,y) plane, is statistically invariant under the scale transformation

$$(x,y,h(x,y)) \rightarrow (\lambda x, \lambda y, \lambda^H h(\lambda x, \lambda y)), \quad (1)$$

where H is the roughness or Hurst exponent. This implies for

example that the width of the surface, measured over an area of size $L \times L$, $w = \sqrt{\langle h^2 \rangle - \langle h \rangle^2}$ scales as L^H .

Slow capillary dominated two-phase flow in two-dimensional horizontally oriented porous media has been studied both experimentally [10,11], and by computer simulations [12–15]. It is now well established that the invasion percolation algorithm reproduces well the structure of the invaded clusters [13,15]. In particular, the fractal dimension [9] of the invasion percolation clusters, $D=1.83$, is consistent with that of the invaded structures in the experiments [10].

Real porous media often display large-scale spatial variations in their properties due to fractures and permeability variations [16,17]. Two phase flow in porous media with long range correlations in the pore size distribution has been studied numerically [18–20]. The fractal dimension of the final structure increases with the degree of spatial correlations. Recent experiments in an open artificial aperture have been compared with an invasion percolation model [21]. In these simulations a threshold value was assigned to each fracture region based on the aperture in that region. The radius of curvature of the fluid interface in the plane of the fracture were, however, neglected. A study of invasion percolation with both curvatures present may be found in Ref. [22].

Gravity affects the structures that form in two-phase flow through buoyancy. When a lighter nonwetting fluid displaces a wetting denser fluid, the structure obtained may be stable [23,24] or unstable (meaning that fingerlike structures develop) [25]. A stable invasion front is observed when the light fluid propagates downwards into the heavier fluid. The unstable situation occurs when the lighter fluid propagates upwards and into the heavier fluid. Fingerlike structures that may fragment are then observed [25–28]. In both situations the structures will have a characteristic width which is controlled by the ratio between the hydrostatic pressure and the

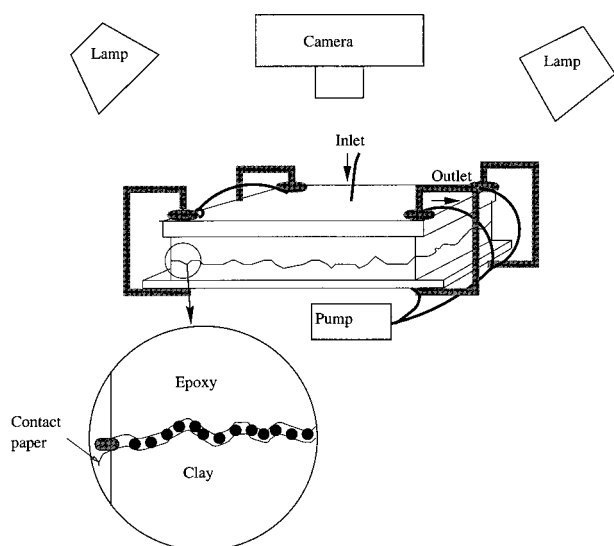


FIG. 1. The experimental setup.

capillary pressure. On a length scale smaller than this characteristic width, the structure has been found to be fractal with a fractal dimension consistent with that of invasion percolation [26].

In our experiment the fracture planes oriented horizontally ensures that both stabilized and fingerlike structures will be present. The monolayer of glass beads introduce capillary pressure fluctuations which have correlations of very short spatial range, as they reflect the pore throat distribution.

In order to approach the regime where buoyancy effects dominate, we have performed experiments in a centrifuge and could in this way increase the “gravitational acceleration” up to $6g_0$. Here $g_0 = 9.8m/s^2$ is the standard acceleration of gravity.

At high values of g , we observe compact “blobs” linked together by stringlike structures. The strings form when less dense fluid propagates upwards, while the blobs form due to gravitationally stabilized downwards motion of the lighter fluid. Fragmentation and migration of the denser fluid were also observed. By decreasing the value of g , the capillary fluctuations become more dominant leading to less compact blobs, with an apparent change in the fractal dimension from $D = 1.98$ to $D = 1.83$.

II. EXPERIMENTS

A. Description of setup and experimental procedure

The experimental model consists of a fracture joint and a porous monolayer (see Fig. 1). The rough surfaces of the joint were obtained by fracturing granite blocks (Lanhelin, Western France) of size $25 \times 25 \times 40 \text{ cm}^3$. To be able to observe optically the structures that form, we made a transparent epoxy casting from the granite fractures. The epoxy model was obtained by first making a silicon cast (rtv 573 A) of the granite fracture, and then making an epoxy cast (Araldite 2020 A and B) from the silicon model. To avoid air bubbles from being trapped in the model, the silicon and the epoxy casts were evacuated for a few hours. Using this procedure we made three pairs of different rough epoxy casts — one from each of the two fracture surfaces that each block

provided. A porous monolayer of glass beads, located between the rough side of the epoxy casting and a contact paper, was forced into contact with the epoxy casting using a block of clay. The purpose of the clay is to be able to obtain a sufficient pressure to maximize the contact between the monolayer and the epoxy plate. A 2 cm thick glass plate was placed on the top of the flat side of the epoxy plate and leveled horizontally. The entire model is on top of a 1 cm thick aluminum plate and is forced together with clamps at the four corners.

When making the model, the clay casting is first made by forcing the clay together with the rough epoxy plate. The clay is then temporarily separated from the epoxy model. The porous monolayer is made by spreading glass beads of diameter $a = 1 \text{ mm}$ onto a contact paper. The contact paper is at this point placed on a flat surface to reduce any spatial correlations in the bead positions due to the roughness of the fracture. The excess of beads are removed and the porous monolayer is placed between the rough epoxy plate and the clay. Spatial correlations due to stretching might be created during this process. However, we believe these to be small and local. To seal the external border of the model we use a silicon glue. Four holes at each corner of the epoxy casting serve as outlets and are connected to the pump. A small hole (0.5 mm) in the middle of the plate forms the inlet.

Three different wetting-nonwetting pairs of fluids were used: Water and air, a glycerol/water mixture and air, and water and silicon oil (Silikonv DC 1107 from KeboLab Norway). The glycerol-water mixture is obtained by mixing 80% of glycerol with 20% of water by weight. The fluids containing water were colored by 0.2 g per liter nigrosine, and degassed to remove air bubbles. The silicon oil was density matched with water to avoid buoyancy effects.

The model was first filled with the colored wetting fluid. A syringe pump (YA-12) was then used to withdraw the liquid at a low flow rate. The experiments were stopped when the invader fluid reached the external boarder of the model. After each experiment the model was either rebuilt or refilled. To check that the refilling procedure did not change the model significantly by trapping of small air bubbles, experiments were repeated under the same conditions after refilling. No significant changes in the structures were observed. This is also an independent check on that there is no deformation of the clay with time. Problems due to clay deformation with centrifuge acceleration was further checked by loading the model with a force corresponding to $12g_0$. No artifacts were observed in the model.

Several of the experiments were performed in a centrifuge at the L.C.P.C. in Nantes, France. The principle of the centrifuge is the following: A basket is rotating on a 5.5 m arm. The effective gravitational force stems from the centrifugal acceleration of the basket. The normal vector to the floor of the basket is always oriented in the direction of the effective acceleration consisting of both the centrifugal and gravitational accelerations. The basket has a length of 1.40 m, a width of 1.15 m, and a height of 1.50 m. This size is large enough to perform the experiments with the camera inside the basket. One can reach a centrifugal acceleration of $200g_0$, but we only ran experiments at an acceleration lower than $7g_0$ in order to prevent damage to the CCD camera. In order to avoid damage to the computer controlling the ex-

periment, it was placed at the rotation center of the centrifuge. The camera, placed inside the basket, was controlled by the computer through a SCSI connection. To receive feedback information from the computer, we made an ethernet connection through slip rings to an external computer placed in the control room.

The displacement process was visualized by illuminating the cell from the sides by four halogen lamps, and pictures were taken from above with a Kodak DCS 420 CCD camera. The images have a resolution of 1536×1024 pixels, and a gray level ranging from 0 to 255. The spatial resolution of the image is 0.06 mm per pixel, or 16 pixels per glass bead. The camera was controlled by a computer which provided a constant time step between each image. Before the experiment started a first image was taken which subsequently was subtracted from all the later images in order to reduce noise. The gray level distribution of the image presents two peaks which corresponds, respectively, to the white and the dark parts of the image. The image is clipped with a threshold set at the minimum between the peaks. The image subtraction procedure was not used for the experiments in the centrifuge because the setup was subject to small vibrations. For these pictures the threshold was adjusted by comparing visually the initial and the thresholded image. Figure 2 shows three of the images for $1g_0$, $3g_0$ and $6g_0$ and the corresponding extracted cluster for $6g_0$.

B. Self-affine properties of fracture

Figure 3(a) shows a gray level representation of the fracture topography. The topography $h(x,y)$ of the epoxy casting was measured by a mechanical profiler [29]. The rough interface was placed on a (x,y) translation table and translated in steps of 0.25 mm between each height measurement. A total of 720 profiles containing 920 heights were obtained.

The rough interface was analyzed by the average wavelet coefficient method [30,31], which is based on the computation of a wavelet transform of the profile $h(x,y)$. In our case we used a two-dimensional version of the method [32], finding that the cast is self affine with a Hurst exponent $H \sim 0.8$ in any direction along the surface. No anisotropies were detected. $H=0.8$ is in good agreement with recent experimental studies of brittle fractures [4–8].

Since the fracture surface is self-affine, the height difference between two pores will increase with the separation between the points. From measurements of $h(x,y)$, we calculated the width w defined as $w = \sqrt{\langle h^2 \rangle - \langle h \rangle^2}$ where the average is over the entire data set, finding $w \approx 2.54a$.

C. Capillary number

The condition for mechanical equilibrium of an interface is given by the Young-Laplace equation

$$P_c = \sigma \left(\frac{1}{R_1} + \frac{1}{R_2} \right). \quad (2)$$

Here R_1 and R_2 are the principal radii of curvatures, and σ is the surface tension. P_c is the capillary pressure drop across the interface. In a porous medium with a characteristic pore throat a , a typical capillary pressure is $P_c \approx 4\sigma/a$. The rela-

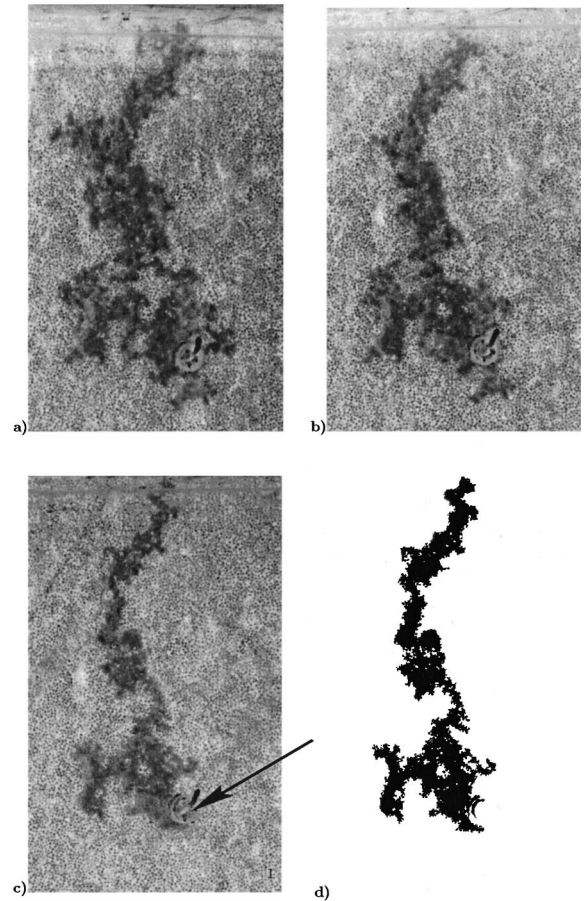


FIG. 2. Example of air clusters (in black) obtained, at the breakthrough, for various $F2w/a$. The gravitational acceleration for (a), (b), and (c) was respectively $1g_0$, $3g_0$, and $6g_0$. The corresponding $F2w/a$ is, respectively, 1.0, 3.1, and 6.1. Between two experiments the cell was refilled with the glycerol-water mixture. The pump rate was $15 \mu\text{l}$ per minute and $C_a = 4 \times 10^{-6}$. Black dots are the beads that form the porous medium. In the bottom of the figures we see the capillary tube by which air enters the cell. The figures cover roughly 25% of the cell. (d) shows the result of the thresholding of figure (c), obtained without using the subtraction technique. The arrow indicates the inlet. The dimension of all pictures are $93 \text{ mm} \times 155 \text{ mm}$.

tive importance of viscous and capillary forces at the pore level is expressed by the capillary number C_a

$$C_a = \frac{\mu U}{\sigma}, \quad (3)$$

where μ is the viscosity of the wetting phase and U is a characteristic flow velocity. In these experiments we define U as $U = L/T$, where T is the duration of the experiment and L the distance between the injection point and the side of the model which is of the order of $100 a$. The physical properties of the fluids are summarized in Table I. The experiments were performed with a flow rate of the order of few μl per minute, and the number of pores invaded per minute was in the range from 1 to 10. This gives capillary numbers in the range from 8×10^{-7} to 5×10^{-6} .

To check if the experiments were sufficiently slow for viscous effects to be neglected, experiments were performed

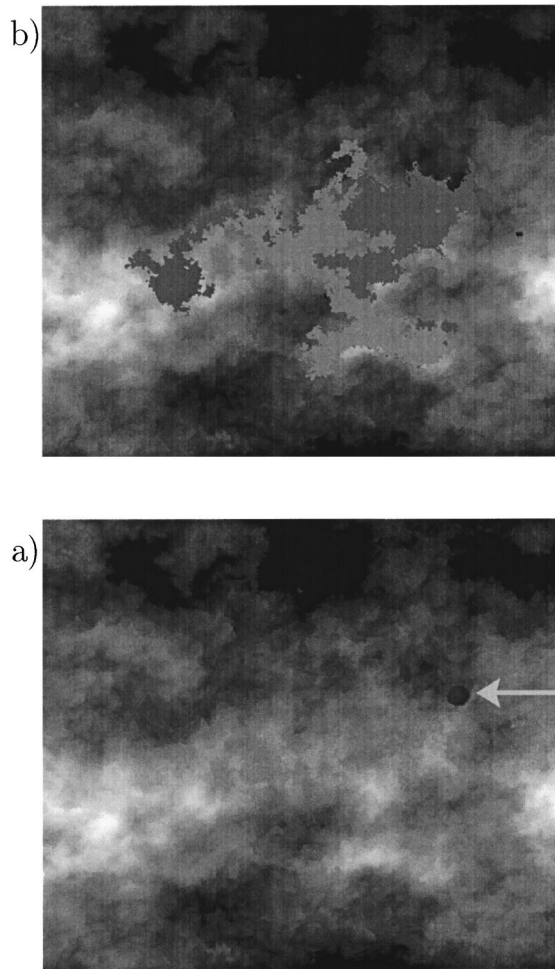


FIG. 3. (b) Grey level representation of the landscape obtained by the needle technique. Highest parts of the cast are presented with light regions. (a) Grey level representation of the landscape with the cluster superimposed on the landscape. The different grey levels of the cluster correspond to the times A , B , C , and D described in the text. The dimension of the picture is $97 \text{ mm} \times 85 \text{ mm}$.

at two different capillary numbers $C_a \approx 8 \times 10^{-7}$ and $C_a \approx 5 \times 10^{-6}$. These experiments were done with the same model (same fracture and porous media) that was refilled. The final structures were not significantly changed between the two experiments, indicating that the injection speed was sufficiently slow.

D. Wetting properties of the fluids

Experiments were performed to check the wetting properties of the fluid pairs by using droplets of one of the fluids

TABLE I. Dynamic viscosity μ , density ρ , and the fluid-fluid surface tension σ of the fluids used at 200 from glycerol-water is a mixture of 20% water and 80% glycerol in mass percent.

	Fluids		
	Water	Air	Glycerol-water
μ [cP]	1.002	0.0190	59.9
ρ [g cm^{-3}]	0.998	0.0116	1.208
σ [dyn cm^{-1}]	73		65

immersed in the other on substrates of glass, contact paper, and epoxy. From these observations we concluded that the pairs air-water, air-glycerol-water mixture and silicon-oil-water are, respectively, nonwetting-wetting pairs. These experiments were performed with the fluids at rest. While changing the acceleration of gravity has no effect on the wetting properties, it is well known that the contact angle changes when the fluid-fluid interface is moving [33]. Two different sets of experiments without buoyancy effects were performed to check that the structures were consistent with the well known structures at low injection rates [10,11]. A deviation from these structures would indicate artifacts in the model or important changes in the wetting properties when the fluids are moving. In a first set of experiments, a model was made with the same materials as before but with a casting of a flat plate rather than a fracture surface. The model was filled either by water or by the glycerol-water mixture and the experiments were performed at a very slow rate $C_a = 10^{-6}$. A second set of experiments performed using the same setup except that the flat surface was exchanged for a rough one. In this latter case the model was filled with water which was displaced by silicon oil. Since these fluids have the same density, gravitational effects were removed. In both series of experiments we observed structures which were similar and consistent with the invasion percolationlike structures observed in experiments on slow drainage in the absence of gravity [10,11]. We obtained fractal dimensions consistent with the fractal dimension $D=1.83$ obtained in previous works [10,11]. This result furthermore supports that the porous medium is kept random and spatially uncorrelated despite modifications that can appear while the porous monolayer is forced between the epoxy print and the clay.

III. COMPETITION BETWEEN GRAVITATIONAL AND CAPILLARY EFFECTS

A. Definition of F

The pore throats in the porous medium have widths that are spatially uncorrelated. Each pore throat exhibits a capillary pressure threshold P_t which corresponds to the minimum capillary pressure needed to penetrate that throat. We designate $N(P_t)$ to be the capillary pressure threshold distribution of the model.

During the experiment, the local pressure in the model will be continuously tuned by the pump. When the pump is running the capillary pressure will increase until one meniscus along the fluid interface becomes unstable, moves through the pore throat and invades the next pore. The condition for this invasion is that the capillary pressure $P_c(x,y)$ at a given throat exceeds the capillary threshold $P_t(x,y)$ of that throat

$$P_c(x,y) > P_t(x,y). \quad (4)$$

In the presence of gravity the capillary pressure $P_c(x,y)$ will depend on the height level due to the hydrostatic pressure. In the following we will define a *reference* capillary pressure $P_r(t)$ at the height $h=0$. $P_r(t)$ is the pressure difference between the invader fluid and the displaced fluid along the interface at a height $h=0$. The capillary pressure

at a given throat on the external perimeter of the cluster is then related to $P_r(t)$ through the formula

$$P_c(x,y) = P_r(t) + \Delta\rho gh(x,y). \quad (5)$$

Here $\Delta\rho$ is defined as the density of the *displaced* fluid minus the density of the *invading* fluid.

Let P^* be the percolation capillary pressure for a flat model. This is the lowest capillary pressure needed to produce a percolating cluster of the invading fluid. The deviation $\Delta P_c(x,y) = P_c(x,y) - P^*$ between the capillary pressure and the critical pressure P^* may then be related to the corresponding quantity for the reference capillary pressure, $\Delta P_r = P_r - P^*$,

$$\Delta P_c(x,y) = \Delta P_r(t) + \Delta\rho gh(x,y). \quad (6)$$

Consider an arbitrary throat and assume that this throat has a meniscus with capillary pressure P_c . The probability p that this throat will be invaded is

$$p = p^* + \int_{P^*}^{P_c} N(P_t) dP_t, \quad (7)$$

where p^* is the occupation probability at the percolation capillary pressure P^* . By assuming that the threshold distribution $N(P_t)$ is slowly varying when P_t is close to P^* , we may substitute $N(P_t)$ for $N(P^*)$ in Eq. (7), giving

$$\Delta p = p - p^* = N(P^*) \Delta P_c. \quad (8)$$

By multiplying Eq. (6) with $N(P^*)$ and using Eq. (8) we obtain

$$\Delta p(x,y) = p - p^* = \Delta p_r(t) + Fh(x,y)/a, \quad (9)$$

where the fluctuation number F is defined as $F \equiv N(P^*) \Delta\rho ga$ and $\Delta p_r(t) \equiv N(P^*) \Delta P_r(t)$. For perfect wetting and a flat capillary threshold distribution over an interval $P_t = 0$ to $P_t = 4\sigma/a$, we have that $N(P^*) = a/4\sigma$, and F is nothing but the bond number $B = \Delta\rho ga^2/4\sigma$. F depends on the wetting properties of the fluids and the width of the capillary threshold distribution w_t which is roughly $w_t \approx 1/N(P^*)$, since $N(P^*)w_t \approx 1$. It is important to note that in general F is different from the bond number B , since it reflects the ratio between the hydrostatic pressure drop on a length scale a and the width w_t of the capillary threshold distribution. The bond number B , however, is the ratio between the hydrostatic pressure drop on a length scale a and the absolute value of a characteristic capillary pressure.

By using Eqs. (4), (6), (8), and (9) the capillary pressures can be mapped onto the occupation probabilities, and the condition for invasion is

$$\Delta p_r(t) + p^* > p_t(x,y) - Fh(x,y)/a. \quad (10)$$

Here $\Delta p_r + p^*$ is a reference level which is continuously tuned by the pump. The next throat to be invaded along the front is the throat with lowest value of $p_t(x,y) - Fh(x,y)/a$. This corresponds to the throat where the capillary pressure first overcomes the capillary threshold value. Equation (10) predicts how this problem can be simulated by an invasion percolation algorithm with long range correla-

tions. In addition to the random numbers $p_t \in [0,1]$ representing the capillary pressure threshold fluctuations an additional term $-Fh(x,y)/a$ should be added representing the variations in the capillary pressure due to the long range correlations in the hydrostatic pressure [34].

B. Measurement of F

The problem in estimating F is that it depends on both the pore size distribution and the wetting properties of the fluids. However, F can be measured at $1g_0$ by performing gravitationally stabilized experiments similar to the experiments described in Ref. [24].

A flat model was prepared and the model was tilted an angle α with the horizontal direction. A tortuous front of front width W propagates from the top to the bottom. The height difference in the model is $\Delta h = \Delta y \sin \alpha$, where Δy is a distance measured in the direction of front propagation. Let $y(t)$ be the front position where the capillary pressure is equal to P^* . This position will move with the speed of the front. Let us now consider the capillary pressure difference between the capillary pressure at the percolation pressure P^* and the capillary pressure at a position $y(t) + W$, where W is the width of the front. The difference in the capillary pressure between these height levels is $\Delta P_c = P_c(y(t) + W) - P^*$, and by using Eq. (8) the corresponding occupation probability Δp is

$$\Delta p = \sin(\alpha) \left(\frac{FW}{a} \right). \quad (11)$$

From percolation theory the correlation length ξ — which measures the typical distance between pores belonging to the same cluster — scales as

$$\frac{\xi}{a} = A \Delta p^{-\nu}, \quad (12)$$

where the prefactor A is of the order of unity [35,36].

In the following we set $A = 1$. By assuming that the width of the front W scales as the correlation length ξ [37], we find

$$F \sin(\alpha) = \left(\frac{W}{a} \right)^{-(\nu+1)/\nu}. \quad (13)$$

This scaling relation has been verified experimentally [24].

For the measurement of F , we used a flat plate made of the same material as the rough fracture plates. A model, for which one side was open, was prepared and filled by the wetting fluid using the method described in Sec. II. The model was then tilted at an angle α , and the wetting fluid was slowly pumped from the lower edge. Air was free to enter the cell from the open upper side. The stable front was recorded by the CCD camera. The width of the front W was defined as the standard deviation of the y position of the front in the direction of propagation

$$W = \langle \sqrt{\langle y^2 \rangle - \langle y \rangle^2} \rangle_t. \quad (14)$$

Here the average $\langle \rangle$ is over all points belonging to one front. The average $\langle \rangle_t$ is over different fronts at different times after the front width has stabilized. We used five different

TABLE II. The width of the front W in unit of bead size a measured for different pairs of fluids and tilt angles α measured in degrees. The fluctuation number F is determined at $1g_0$ using Eq. (11). The bond number $B = \Delta\rho g a^2 / 4\sigma$ at $1g_0$ is calculated from Table I.

Nonwetting-wetting fluids	α	W/a	$\Delta W/a$	F	ΔF	B
Air-water	4.82	13	2	0.13	0.03	0.034
Air-water	1.62	25	2	0.13	0.02	0.034
Air-glycerol-water mixture	1.62	19	6	0.20	0.05	0.046

fronts. F was calculated using Eq. (13). The uncertainty in the front width ΔW was estimated as the maximum deviation of the set of W measurements. Table II lists F determined in three experiments. We estimate $F = 0.13$ for the pair air-water and $F = 0.20$ for the pair air-glycerol-water mixture at $1g_0$.

C. Characteristic length scales

In the porous model there are two characteristic length scales, the pore size a and the system scale L . Let w be the amplitude of the fracture at the system size L . On large scales the gravitational effects dominate when $F2w/a > 1$. Note that a characteristic width of the fracture is two times the amplitude w which explains the factor 2 above. The capillary effects start to be important on the system size when $F2w/a \approx 1$. Since w/a scales as $w/a = (w_a/a)(L/a)^H$, where w_a is the characteristic width at the pore scale, this defines a length scale ζ as

$$\zeta/a = (F2w_a/a)^{-1/H}. \quad (15)$$

On length scales smaller than ζ the capillary effects start to be important. On the pore scale, the capillary effects will dominate when $F2w_a/a \ll 1$. However when $F2w_a/a \gg 1$, there are no effect of capillary fluctuations and the flow is completely controlled by the gravity. At the highest g in our experiments we obtain $F2w/a = 6.1$ and $F2w_a/a = 0.09$. This means that gravity effects dominate on large scales and are small but present even at the pore scale.

There are various manners to experimentally tune $F2w/a$. The first one is to change the model size. Since $w \sim L^H$, an increase of the system size will expand w . However, if the system size L is increased by a factor 2, w is only increased by a factor $2^H = 1.7$. Another way is to change the fluids used, this will modify $\Delta\rho$, μ , and σ . However, as can be seen in Table II, F does not vary significantly with the fluid couples used. Another possibility is to tune the ‘‘acceleration of gravity’’ by running experiments in a centrifuge. We found that this was the easiest way for changing F . This procedure also has the advantage of keeping the physical parameters of the fluids ($\sigma, \Delta\rho, \mu$) constant.

By performing experiments with various pairs of fluids and accelerations, we achieved a set of six different $F2w/a$: 0, 0.66, 1.0, 3.1, and 6.1. $F2w/a = 0$ corresponds to the experiments described in Sec. II D in which the fluids (water and silicon oil) were density matched. $F2w/a = 0.66$ is obtained at $1g_0$ when the pair of fluid used is air water. $F2w/a = 1.0$ is achieved at $1g_0$ for the pair air-glycerol-water mixture. $F2w/a = 3.1$ and 6.1 are obtained when the pair air-glycerol-water mixture is used at respectively $3g_0$

and $6g_0$. Table III lists for each value of $F2w/a$, the number of experiments, the number models constructed for each fracture, and the number of different fractures used.

IV. RESULTS

A. Experiments at different g

Figure 2 shows three different clusters at the point of breakthrough for the same model (fracture and porous media) but different accelerations $1g_0$, $3g_0$, and $6g_0$ corresponding to $F2w/a = 1.0$, 3.1, and 6.1. The boundary of the structure becomes smoother at increased g indicating that the capillary fluctuations are increasingly suppressed. For the $6g_0$ experiment, the structure is composed of parts which look like compact blobs connected with tiny structures or ‘‘strings.’’ It is also clear from this figure that the mass of structures is reduced as g is increased. However, it is important to note that this is not true for all models, and depends on the choice of the injection points.

The invaded structure was correlated with the underlying topography $h(x, y)$. By using four marks on the corners of the model as reference points, the images were rotated and rescaled until the marks correspond with the same marks measured by the mechanical profilometer. In this way, it was possible to superimpose the clusters on the fracture topography $h(x, y)$. The average height of the cluster

$$\langle h \rangle = \frac{\sum_{i,j} h(i,j) O(i,j)}{\sum_{i,j} O(i,j)}, \quad (16)$$

was measured for the different experiments. The zero level of the heights has been chosen such that $\langle h(i,j) \rangle = 0$. $O(i,j)$

TABLE III. List of all the experiments performed for various $F2w/a$. The columns, respectively, give $F2w/a$, the name of the wetting fluid, the name of the nonwetting fluid, the number of experiments, and the number of different fracture used. W is water, G is glycerol-water mixture, A is air, and S is silicon oil.

$F2w/a$	WF	NWF	g/g_0	No. of expt.	No. of fractures
	W	A		1	flat cell
0	G	A	1	1	flat cell
	W	S		1	fracture
0.66	W	A	1	3	2
1.0	G	A	1	6	4
3.0	G	A	3	3	3
6.1	G	A	6	3	3

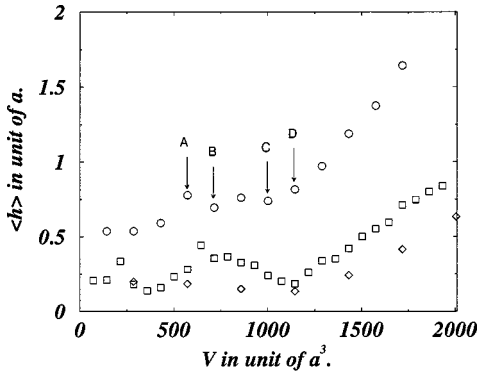


FIG. 4. Average height of the region occupied by the nonwetting phase as function of the injected volume V . Circles, squares, and diamonds represent, respectively, the $\langle h \rangle$ for $F2w/a = 6.1, 3.1,$ and 1.0 . The injected volume between two pictures in units of average pore volume is 286, 72, and 143 for, respectively, $F2w/a = 1.0, 3.1,$ and 6.1 . This corresponds to a time delay between figures of 10, 2.5, and 5 min. The points A, B, C, and D show the average heights of cluster represented in Fig. 3.

is one if the thresholded pixel (i, j) belongs to the invaded cluster and zero otherwise. Figure 4 shows $\langle h \rangle$ as function of the injected volume V for the three different experiments. When $F2w/a$ is increased, the invaded region is found preferentially in higher parts of the topography. However, in the figure there are domains where $\langle h \rangle$ increases and domains where $\langle h \rangle$ decreases with V . Let us consider the shape of the clusters obtained at the point A and B of Fig. 4. Between these two points $\langle h \rangle$ has decreased, and the structure is growing downwards. Figure 3 shows the cluster at the two points A and B. The structure generated between A and B is compact with very few trapped islands. Let us now focus on the points C and D shown on Fig. 4. In this case $\langle h \rangle$ has increased. We furthermore see in Fig. 3 that the new structure looks like a “string” with a small blob at the end. When the invader fluid reaches the top of a hill it develops by going downhill in a stable way. After some time the structure reaches the bottom of the valley, and the cluster then grows uphill in a stringlike way. When a high peak is reached again, the cycle is repeated, a blob is generated by going downhill and incorporating parts of the string.

B. Fractal dimension of the invaded region

Two-phase flow in porous media often give rise to complex structures which are fractal. The structures observed in our experiments are indeed complex, but for high values of $F2w/a$, the structures are not “simple” fractals. The structures consist of blobs connected by strings. The internal part of the blobs looks compact and the strings are essentially one dimensional. Analyzing these structures by traditional fractal methods such as the box counting method or the radial mass method [38] yields poor scaling for high values of $F2w/a$. To emphasize on the structures inside the blobs, a method called the inside mass method has been developed. Let us first define the external perimeter of the cluster as all invader sites having at least one of their closest neighbors as a non-trapped defender site. In this method each pixel i on the cluster is chosen and the mass $m_i(r)$ within the distance r from i is calculated. Only distances shorter than the shortest

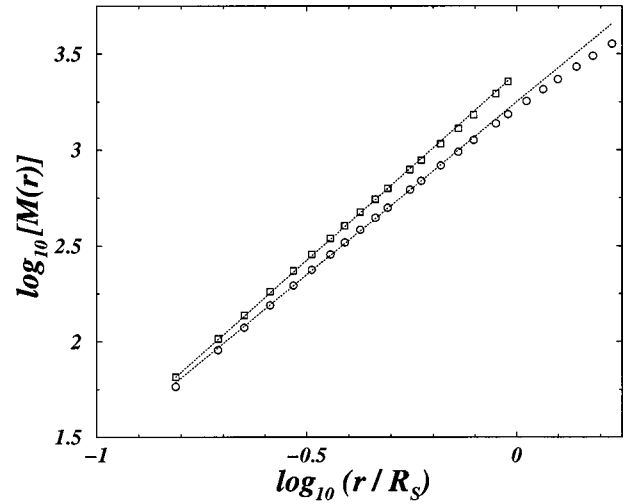


FIG. 5. Dependence of $M(r)$ on r/R_s . Squares represent the result of the inside mass method applied on the cluster shown in Fig. 2(c). The result obtained by a classical method, here the average mass, on the same cluster is represented by circles. The dotted lines have a slope of 1.95 and 1.80. In this system $F2w/a = 6.1$.

distance to the external perimeter r_i are considered in the calculations. Then the average mass $M(r)$ is calculated as

$$M(r) = \frac{\sum_i m_i(r) \theta(r_i - r)}{\sum_i \theta(r_i - r)}, \quad (17)$$

where $\theta(x)$ is the Heaviside step function which is equal to 0 for $x < 0$, and 1 for $x \geq 0$. This method emphasizes on the structure inside the external perimeter of the cluster and the average mass is expected to behave as

$$M(r) = Kr^D, \quad (18)$$

for $r < R_s$, where R_s is the radius of the biggest circle that can be inscribed inside the external perimeter of the clusters.

In Fig. 5, $\log M(r)$ is plotted as function of $\log(r/R_s)$ for $F2w/a = 6.1$. By fitting to a linear curve with r/R_s in the range from a/R_s to 1.0, we find $D = 1.95$ close to a compact structure. To compare this result with the traditional ways of measuring the fractal dimensions, the average mass $M_i(r) = \sum_i m_i(r) / M_{\text{tot}}$ were calculated where M_{tot} is the total mass of the cluster. The only difference in this case is that r can take all values without any upper limits r_i of r . By fitting the data to a linear curve with r/R_s in the range from a/R_s to 1, we find an “effective” dimension $D = 1.80$. However, it is important to note that this line is curved, and that the result will strongly depend on the fitting range. The last method gives an apparent dimension which is underestimated and does not reflect the compact structure inside the external perimeter.

For each experiment we have computed the mass $M(r)$ at breakthrough. The average $\langle M(r) \rangle$ over all clusters obtained at breakthrough was then computed for the different $F2w/a$. The fractal dimension D was found by fitting $\log \langle M(r) \rangle$ versus $\log(r/R_s)$ to a linear function with r/R_s in the range from a/R_s to 1. The results are presented in Table IV. Figure 6

TABLE IV. Fractal dimension of the structures at the breakthrough for various $F2w/a$. D_{fit} is the slope of the linear regression of the $\log_{10}(\langle M(r)/R_s \rangle)$ within a window starting at the pore level and ending at $r/R_s=1$. ΔD_{fit} is the maximal deviation of the slope of a single set from D_{fit} .

$F2w/a$	D_{fit}	ΔD_{fit}
0	1.83	0.03
0.66	1.85	0.02
1.0	1.91	0.03
3.1	1.98	0.01
6.1	1.96	0.03

shows $\log[\langle M(r) \rangle]$ as function of $\log(r/R_s)$ for different values of $F2w/a$. It is important to note that the system is small and that D values are effective exponents found by assuming a power law behavior. We checked by varying the clip level by 5% from the minimum in the gray level distribution that it does not influence the fractal dimension.

We note that while $F2w/a$ increases the fractal dimension increases from 1.83 to 1.98. In other words, when the hydrostatic effect is increased the inside structure of the blobs becomes more and more compact.

C. Trapping effect and saturation

The effect of trapping has been studied by measuring the ratio ϱ of the number of trapped pixels describing trapped islands of invader and the number of pixels belonging to the cluster. In Fig. 7 is shown the average of ϱ at breakthrough at different $F2w/a$. We see that ϱ decreases while the hydrostatic effect is increased, which means that the number of trapped islands becomes smaller.

Saturation is often used to characterize the invasion of a porous medium. Let us define saturation S as the ratio between the number of black pixels representing the cluster and the total number of pixels representing the model. For a

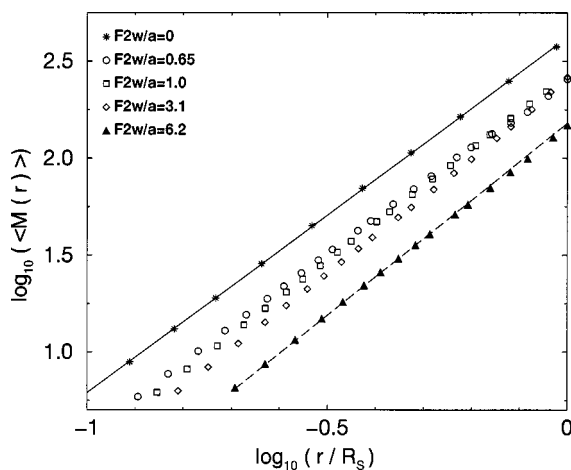


FIG. 6. $\log(\langle M(r) \rangle)$ as a function of $\log(r/R_s)$ where $\langle M(r) \rangle$ is the average of $M(r)$ over clusters obtained at the breakthrough for a given $F2w/a$. Circles, diamonds, squares, triangles up and left are, respectively, for $F2w/a=0, 0.66, 1.0, 3.1,$ and 6.1 . The solid line is a linear fit with $D=1.83$ for $F2w/a=0$. The dashed line is a linear fit with $D=1.98$ for $F2w/a=6.1$.

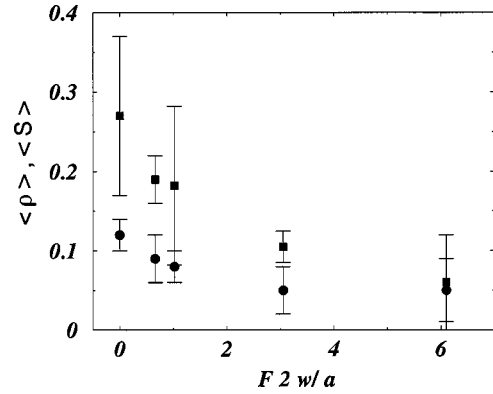


FIG. 7. Squares show the mean ratio $\langle \varrho \rangle$ as function of $F2w/a$. The assessment of ϱ is done at the breakthrough, and is then averaged over all the experiments done at a given $F2w/a$. Vertical bars indicate the maximal deviation of ϱ from $\langle \varrho \rangle$. Circles show the mean saturation $\langle S \rangle$ at the breakthrough for different $F2w/a$, obtained by averaging all the saturation found over all the set of experiment. Vertical bars show the maximal deviation from the mean saturation.

given $F2w/a$, we have computed the mean saturation S at breakthrough. The result is shown in Fig. 7, where we observe that S decreases when the buoyancy difference increases.

D. Fragmentation and migration

Fragmentation and migration occur when a light non-wetting fluid propagates upwards in a denser wetting fluid. These phenomena have recently been observed in drainage experiments [25,27]. We also observed fragmentation in our experiments at $6g_0$ when the injection point, indicated by the arrow (2) in Fig. 8, was located at the lowest point of the fracture interface. A stringlike structure developed upwards towards higher levels in the landscape. When the height difference between the highest and the lowest invaded pore increases, the capillary pressure at lower levels become sufficiently small such that the menisci retract. This retraction or inhibition step might lead to fragmentation of the structure. The retraction occurs when the capillary pressure difference between two points along the cluster due to the hydrostatic pressure drop $\Delta p g \Delta h$ becomes of the order of the characteristic capillary pressure $4\sigma/a$. The length scale Δh is controlled by the Bond number through $\Delta h/a \approx 1/B$. At $6g_0$, the height difference $\Delta h/a \approx 1/B=3.6$, and fragmentation effects are expected to be important. Figure 8 shows the fragmented structures. Snap off occurred usually at lower-lying positions on the strings and bubbles become mobile and moved until stable positions were reached. Consider the moving bubbles which is indicated by the arrow (1) in Fig. 8. We found that the bubble has covered a distance of $14a$ during 40 min which corresponds to $C_a=6 \times 10^{-6}$. This indicates that viscous effects are not important during migration. During migration bubbles sometimes coalesce. Figure 9 shows two bubbles just before they touch and then the final situation where only one bubble remains. We see that the head of the final bubble has expanded while the back part has been retracted. The expansion of the head is about 100 pores and the duration of this process is of the order of 5 min. The

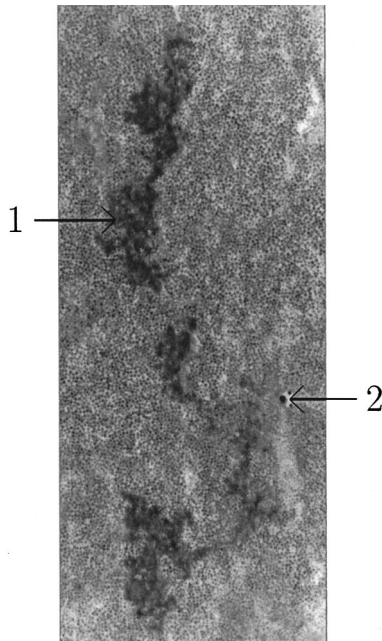


FIG. 8. Fragmentation of the air bubbles. The injection point indicated by the arrow (2), is located at the lowest point of the fracture. The experiment has been run under an acceleration of $6g_0$ ($F2w/a=6.1$) and with $C_a=2\times 10^{-6}$. The size of the image is $85\text{ mm}\times 205\text{ mm}$ and the injected volume is $3578a^3$. The arrow (1) indicates a moving bubble.

capillary number associated with the coalescence is of the order of $C_a=4\times 10^{-3}$, showing that viscous effects are present. The capillary number was estimated using Eq. (3) where the flow velocity U was determined by comparing consecutive images of the process.

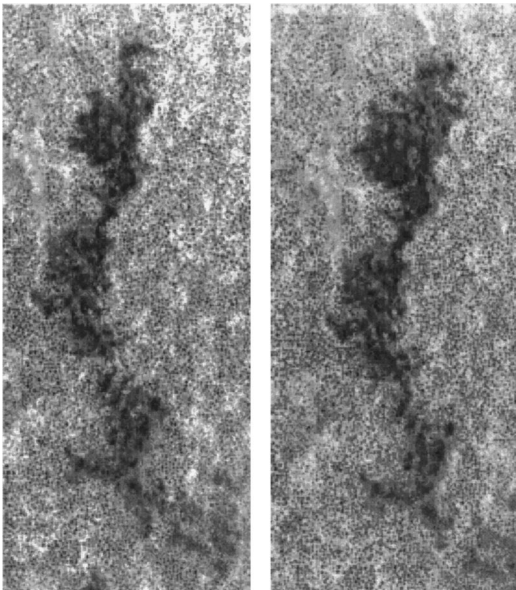


FIG. 9. Coalescence of two air bubbles. The left image shows the bubbles just before the coalescence. The right image represents the final bubble 5 minutes after. The experiment has been run under an acceleration of $6g_0$ ($F2w/a=6.1$) and with $C_a=2\times 10^{-6}$. The size of the image is $57\text{ mm}\times 137\text{ mm}$ and the injected volume is $5725a^3$.

After the migration, a long period of stagnation occurs during which some of the strings are refilled. Blobs are then reconnected to the inlet with a corresponding increase in height difference between the highest point of the front and the injection point. When the height difference between the highest and the lowest point become sufficiently high, the menisci retract and the structure fragment again. A new cycle of fragmentation, migration, and coalescence then starts.

V. DISCUSSION

As discussed in Sec. III the condition for invasion of a pore is that the local capillary pressure is greater than the capillary pressure threshold of that pore. Due to the fracture topography the capillary pressure will increase with height [Eq. (5)]. The throat which is invaded next is the one which has a capillary pressure which is closest to the capillary pressure threshold value of the just invaded throat. The pumping will increase the capillary pressure with time with the same contribution over the hole model until the pore with the lowest value of $p_i(x,y)-Fh(x,y)/a$ becomes unstable and is invaded. For large values of $F2w/a$, the growth process will be dominated by the gravitational effects, and it is much more favorable to grow at high positions in the landscape than at low positions. This means that if the injection starts in a low valley of the landscape, the cluster will grow in the direction of the largest gradient of $h(x,y)$ and generate stringlike structures. The local width of the strings is controlled by the strength of the capillary fluctuations and will decrease with an increased gradient of $h(x,y)$ and an increased value of $F2w/a$. These structures have recently been studied for a simple two-dimensional tilted plane [27,28] and similar structures have been observed in three dimensions [25]. In the opposite situation, when the cluster develops downwards from a high ‘‘mountain’’ gravitationally stabilized structures will appear. The width of the front is controlled by the capillary fluctuations, and will decrease with the gradient of $h(x,y)$ and the value of $F2w/a$. In the limit of large $F2w/a$ we therefore expect strings which connect compact areas or blobs. Both unstable and stable invasions process lead to a decrease of the number of trapped pores when buoyancy grows. In our system we found that the saturation is reduced when $F2w/a$ increases. This effect is related to the presence of links that drive the invasion in preferred directions. However, it is important to note that this effect is expected to depend on the particular model and the choice of injection point as well.

The analysis of the structures by calculating the fractal dimension with usual fractal methods as the box counting or radial mass method is misleading at high values of $F2w/a$. Typically these methods will give a fractal dimension which is underestimated with a value close to the invasion percolation results. We found that the inside mass method was a proper way of analyzing the internal part of the clusters, i.e., structures on a length scale smaller than the size of the largest blob.

For gravitationally stabilized drainage, in a two-dimensional porous media, the width of the front W is found to decrease with F [24]. However, on length scales smaller than the width of the front the structure will still remain

fractal with the same fractal dimension D . This is contrary to what is observed in the present experiment with long range correlations. By applying the inside mass method a significant change in D was observed on length scales smaller than the R_s . As seen in the experiments the ‘‘apparent’’ fractal dimension of the internal structure change from $D=1.83$, in the capillary dominated regime, to $D=1.98$ in the gravity dominated regime. The compact behavior of the internal structure can be seen by visual inspection. When the gravity effects become dominant, the external perimeter around the blobs will follow constant height levels in the landscape without the strong capillary fluctuations creating trapping at low F . Many of the internal peaks in the fracture landscape will also be invaded by gravitationally stabilized drainage following after a ‘‘string’’ reaches the top of the peak. In the capillary dominated regime it is well known that the structures are fractal with a fractal dimension $D=1.84$ [10] consistent with the results of invasion percolation [13].

It is of great interest to analyze the size distribution of the blobs. However, due to limited statistics, it is not possible to study this in our experiments. In Sec. III we argued that the problem can be mapped onto an invasion percolation process by long range correlations due to the self-affine fracture landscape. Studies of the scaling properties of the links and the blobs using the correlated invasion percolation simulation (Sec. III) is one of the issues of Ref. [34]. Wagner *et al.* [19] have studied the scaling properties of correlated invasion percolation and found that distribution $N(m)$ of the blob masses m scaled as $N(m) \sim m^{-1.3}$ for $H=0.8$. In these studies the noise was purely self-affine with no additional white noise. In the limit of large g the dominant noise term in our

problem is also purely self-affine, and the blob distribution is expected to follow the scaling law $N(m) \sim m^{-1.3}$ as shown in Ref. [34].

At increased gravity or increased system size there will always be a regime where fragmentation effects becomes important. This will appear when the hydrostatic pressure difference between two points on the external perimeter of the cluster overcomes the typical capillary threshold value. It is important to note that snap-off effects will depend on the absolute value of the average capillary pressure threshold through the Bond number B . At the experiments of $6g_0$ we clearly observed fragmentation and migration effects of the clusters. The incorporation of the fragmentation effect into an invasion percolation simulation have been successfully performed by Wagner *et al.* [39]. In Ref. [34], we used a similar algorithm to include fragmentation in the invasion percolation simulation.

ACKNOWLEDGMENTS

We thank Eirik Grude Flekkøy, Irene Ippolito, Grunde Løvoll, Paul Meakin, Stephane Bourles, Stephane Roux, and Geri Wagner for stimulating and useful discussions. We thank the LCPC for facilitating our access to the Nantes centrifuge (Information on the LCPC centrifuge may be found at <http://www.lcpc.inrets.fr/LCPC/Moyens.equipements/Equipements/Centrifugeuse>.) We are grateful to the CNRS and NFR for support through the Franco-Norwegian *PICS* program, Grant No. 753. One of us (H.A.) would like to thank the Secretariat of the Cultural Exchange Programs (K.A.S.) and the Research Council of Norway for financial support.

-
- [1] F. Dullien, *Porous Media, Fluid Transport and Pore Structure* (Academic Press, San Diego, CA, 1979).
- [2] M. Sahimi, *Flow and Transport in Porous Media and Fractured Rock* (VCH, Weinheim, 1995).
- [3] M. Sahimi, Phys. Rep. **306**, 213 (1998).
- [4] B. Mandelbrot, D. Passoja, and A. Paullay, Nature (London) **308**, 721 (1984).
- [5] E. Bouchaud, G. Lapasset, and J. Planeès, Europhys. Lett. **13**, (1990).
- [6] K. Måløy, A. Hansen, and E. Hinrichsen, Phys. Rev. Lett. **68**, 213 (1992).
- [7] C. Poon, R. Sayles, and T. Jones, J. Phys. D **25**, (1992).
- [8] E. Bouchaud, J. Phys.: Condens. Matter **9**, 4319 (1997).
- [9] B. Mandelbrot, *The Fractal Geometry of Nature* (W.H. Freeman, New York, 1982).
- [10] R. Lenormand and C. Zarcone, Phys. Rev. Lett. **54**, 2226 (1985).
- [11] K. Måløy, F. Boger, J. Feder, and T. Jøssang, in *Time-dependent Effects in Disordered Materials*, edited by R. Pynn and T. Triste (Plenum Press, New York, 1987).
- [12] R. Chandler, J. Koplik, K. Lerman, and J. Willemsen, J. Fluid Mech. **119**, 249 (1982).
- [13] D. Wilkinson and J. Willemsen, J. Phys. A **16**, 3365 (1983).
- [14] L. Furuberg, J. Feder, A. Aharony, and T. Jøssang, Phys. Rev. Lett. **61**, 2117 (1988).
- [15] R. Lenormand, E. Touboul, and C. Zarcone, J. Plasma Phys. **189**, 165 (1988).
- [16] A. Katz and A. Thompson, Phys. Rev. Lett. **54**, 1325 (1985).
- [17] T. Hewett (unpublished).
- [18] L. Paterson, S. Painter, M. Knackstedt, and W. Pinczewski, Physica A **233**, (1996).
- [19] G. Wagner, P. Meakin, J. Feder, and T. Jøssang, Phys. Rev. E **55**, 1698 (1997).
- [20] M. Sahimi and S. Mukhopadhyay, Phys. Rev. E **54**, 3870 (1996).
- [21] H. Amundsen, G. Wagner, U. Oxaal, P. Meakin, J. Feder, and T. Jøssang, Water Resour. Res. (to be published).
- [22] R. Glass, M. Nicholl, and L. Yarrington, Water Resour. Res. **34**, 3215 (1998).
- [23] E. Clement, C. Baudet, and J. Hulin, J. Phys. (France) Lett. **46**, L (1985).
- [24] A. Birovljev *et al.*, Phys. Rev. Lett. **67**, 584 (1991).
- [25] V. Frette, J. Feder, T. Jøssang, and P. Meakin, Phys. Rev. Lett. **68**, 3164 (1992).
- [26] P. Meakin *et al.*, Physica A **191**, 227 (1992).
- [27] A. Birovljev *et al.*, Phys. Rev. E **51**, 5911 (1995).
- [28] G. Wagner *et al.*, Phys. Rev. E **55**, 7015 (1997).
- [29] J. López and J. Schmittbuhl, Phys. Rev. E **57**, 6405 (1998).
- [30] A. Mehrabi, H. Rassamdana, and M. Sahimi, Phys. Rev. E **56**, 712 (1997).
- [31] I. Simonsen, A. Hansen, and O. Nes, Phys. Rev. E **58**, 2779 (1998).
- [32] I. Simonsen and A. Hansen (unpublished).

- [33] N. Morrow, *J. Can. Pet. Technol.* **15**, 49 (1976).
- [34] J. Schmittbuhl, A. Hansen, H. Auradou, and K. Måløy (unpublished).
- [35] D. Stauffer, *Phys. Rep.* **54**, 1 (1979).
- [36] B. Sapoval, M. Rosso, and J. Gouyet, *J. Phys. (France) Lett.* **46**, L149 (1985).
- [37] D. Wilkinson, *Phys. Rev. A* **30**, 520 (1984).
- [38] J. Feder, *Fractals* (Plenum, New York, 1988).
- [39] G. Wagner, P. Meakin, J. Feder, and T. Jøsang, *Physica A* **245**, (1997).